Ce-doped bundled ultrafine diameter tungsten oxide nanowires with enhanced electrochromic performance

Kunyapat Thummavichai,[a] Fang Xu,[b] Nigle Neate,[b] Nannan Wang,[a] Adolfo De Sanctis,[a] Saverio Russo,[a] Shaowei Zhang,[a] Yongda Xia,[a] and Yanqiu Zhu[a,*]

[a] *College of Engineering, Mathematics and Physical Sciences, University of Exeter EX4 4QF, UK*

[b] *Advanced Materials Group, Faculty of Engineering, The university of Nottingham, Nottingham NG7 2RD, UK*

* Author to whom correspondence should be addressed. Electronic mail: y.zhu@exeter.ac.uk

Abstract

Cerium (Ce)-doped tungsten oxide nanostructures were synthesised using a simple solvothermal method from cerium chloride salt ($CeCl_3 \cdot 7H_2O$) and tungsten hexachloride (WCl_6) precursors. As-prepared samples were thoroughly characterised using electron microscopies, x-ray diffraction (XRD), x-ray photoelectron spectroscope (XPS) and Raman. The electrochromic performance of different samples was evaluated using a custom-built UV-VIS spectrometer and electrochemistry technique. The results showed that the as-prepared samples underwent morphological evolutions with increasing the Ce/W molar ratios, from long, thin and bundled nanowires, through shorter and thicker nanowires to mixed nanowire bundles and nanoparticle agglomerates. From electrochemical testing, we found that the Ce-doped tungsten oxides exhibited higher optical contrasts of 44.3%, 49.7% and 39.4% for the 1:15, 1:10 and 1:5 Ce/W ratio respectively, compared with 37.4% of the pure $W_{18}O_{49}$ nanowires. The Ce/W = 1:15 samples presented an improved colouration efficiency of 62 cm^2/C

26   against 51 cm^2/C of pure $W_{18}O_{49}$. This work demonstrated that the Ce-doped $W_{18}O_{49}$ nanowires are

27   very promising candidate materials for the design and construction of electrochemical chromic

28   devices with largely improved efficiency, contrast and stability. The results from this work suggested

29   that smart electrochromic devices based on current Ce-doped WO_x nanomaterials could be further

30   developed for future energy-related applications.

Introduction

Tungsten oxide (WO_x) nanoparticles have been extensively studied as an important class of electrochromic materials, because of their advanced features including high colouration efficiency, high cyclic stability, low power consumption, good memory effect and high contrast ratios,[1,2] compared with other transition metal oxides. Non-stoichiometric forms of WO_x, ($2 \leq x \leq 3.1$), in particular, the most notable ones such as $W_{18}O_{49}$ nanorods or nanowires exhibit larger specific surface area than their spherical nanoparticles counterparts.[3-5] These non-stoichiometric structures could lead to even better electrochromic performance than saturated WO_3 nanoparticles, since the non-stoichiometric composition in the lattice, which could have more intrinsic oxygen vacancies and revised crystal structure that offer more active sites for accommodating potential doping metals and alkaline ions, which facilitate the electrochromic effect.[6] Recently, we have synthesised ultrafine bundled $W_{18}O_{49}$ nanowires, with only 2-4 nm in individual nanowire diameters and a record high specific surface area over 150 m^2/g.[7] Such long and thin nanowires could be a potential candidate material for chromic applications.

Metallic dopants introduced into the lattice of WO_x have been proven to be able to improve chromic properties, via promoting the formation of coloration centres of W^{5+} from either W^{4+} or W^{6+}, or both. Various heteroatoms have been introduced into WO_x for this purpose, including Erbium (Er),[8] Lanthanum (La),[9] Praseodymium (Pr),[10] Yttrium (Y),[11] Cerium (Ce),[12-15] etc. Amongst various rare-earth metals, Ce has received the most attention in doping or coupling of different oxide semiconductors for enhanced chemical, optical, optoelectric and luminescent properties.[12] Ce-doped compounds, *e.g.* CeO_2 and $CeWO_6$, exhibit interesting characteristics for oxygen storage and release *via* a redox shift between Ce^{4+} and Ce^{3+} under oxidation and reduction conditions.[16] This could also lead to the state change of the base oxide (WO_x) and result in efficient coloration. So far, the electrochromic performances of Ce-doped WOx have been barely studied, there have been only a few reports focusing on Ce doping of other transition metals rather than tungsten. For example, using a

57 simply sol gel method,[17] Dhanasankar prepared a Ce-MoO$_3$ structure with improved electrochromic

58 performance and high stability, in terms of coloration efficiency and variation in transmission

59 between the coloured and bleached states. CeO$_2$-TiO$_2$ also showed a better colouration efficiency of

60 231 cm^2/C when it was used as the counter electrode for a WO$_3$ device.[18,19] Furthermore, Ce-TiO$_2$,[20]

61 Ce-WO$_x$,[21] and complex structures of Ce-V$_2$O$_5$WO$_3$/TiO$_2$ showed improved performances than their

62 parental oxides alone, *e.g.* as a catalyst for highly efficient reduction of NO$_x$ emission from the diesel

63 exhaust. In addition, Ce-NiO nanostructures exhibited excellent electro-catalytic and bio-medical

64 performances toward the detection of riboflavin (RF).[22] Therefore, exploring Ce doping of WO$_x$ and

65 the suitability of this system for electrochromic applications is of scientifically importance.

66

67 Inspired by the interesting features that Ce could bring to other metal oxides, we combined the unique

68 W$_{18}$O$_{49}$ nanowires of ultrafine diameter with the promising effect of Ce doping, and assessed the

69 influence of such a combination on the overall electrochromic performance. In this study,

70 morphological and structural changes of Ce-doped WO$_x$ nanowires during the solvothermal synthesis

71 process were initially investigated in detail, which was followed by the evaluation of their potentials

72 and performance improvements in electrochromic devices, in comparison with the non-doped pristine

73 W$_{18}$O$_{49}$ nanowires. This study would allow us to gain an in-depth understanding about the Ce-doped

74 WO$_x$ functional nanostructures, which could be used as a guideline for structure modification and

75 smart functional device development of these WO$_x$-based materials, towards energy-related

76 technological applications, such as chromic smart windows, sensors, catalysis, and intelligent solar

77 cell protections.

78

79 **Experimental**

80 *Nanowire synthesis*

81 The pristine bundled W$_{18}$O$_{49}$ nanowires were synthesised by following a solvothermal process

82 reported earlier.[7] Tungsten hexachloride (WCl$_6$) and cyclohexanol were used respectively as the main

precursor and the solvent. In a typical synthesis, a certain amount of WCl_6 was dissolved in the cyclohexanol to form a 0.003 M solution. 50 ml of the solution were transferred to a 120 ml Teflon-lined stainless steel autoclave which was sealed before being heated at 200 °C for 6 h in an oven. For Ce-doped WO_x samples, a mixture of $CeCl_3 \cdot 7H_2O$ and WCl_6 was initially dissolved in 1 ml of ethanol in a beaker to obtain a solution, 49 ml of cyclohexanol were then added into the beaker and further mixed under ultra-sonication for 15 min. The resultant homogeneous solution was subsequently transferred to the Teflon-lined stainless steel autoclave. The reaction vessel was sealed before being heated at 200 °C for 10 h in the same oven. The actual molar ratios of $CeCl_3 \cdot 7H_2O$ and WCl_6 were 1:15, 1:10 and 1:5, respectively. After heating, the autoclave was oven-cooled to room temperature. All the product samples were washing with deionized water, ethanol and acetone, and centrifugally collected. The collected product samples were oven-dried at 80 °C for 12 h prior to further characterisation and testing.

Thin film preparation

The thin film for subsequent electrochromic testing was prepared by a spin coating of a nanowires suspension. The latter was obtained from dispersing 0.1 g of different nanowires ultrasonically in 2 ml ethanol. The suspension was then dropped immediately onto a 25 mm × 25 mm × 1 mm ITO (Indium Tin Oxide) coated substrate sitting inside the spin coater. The spin coater was set up at 1200 rpm for 5 s in the first step, and continued to spin at 1500 rpm for a further 5 s. Each sample was re-coated for 10 rounds, and eventually a good and uniform coverage of desired film thicknesses was achieved. The film was then oven-dried at 100 °C for several hours. As for the thin films selectively used to evaluate the crystallinity influence (see Section 2 below), they were pre-treated at 300 °C for 2 h under 100 sccm of Ar flow in a tube furnace. The film thickness was measured, using an optical Profilometry technique, as around 400 nm on average in all samples.

Sample characterisation

Phases of films coated on the ITO conducting glass were identified by X-ray diffraction (XRD) measurements which were obtained using a Bruker D8 Advance diffractometer, with a Cu $K\alpha$ radiation (operated at 40 kV – 40 mA) at a time interval of 1 s and a step size of 0.02°, within the 2θ range from 20 to 60°. Structures and morphologies of the films were examined using a scanning electron microscopy (SEM) (Philips XL-30) operate at a voltage of 20 kV, and a high resolution transmission electron microscope (HR-TEM) (JOEL-2100) at 200 kV acceleration voltage. X-ray photoelectron spectra (XPS) were recorded using a VG ESCALab Mark II spectrometer with non-monochromatic Al-anode x-ray source (1486.6 eV), operated at a 12 kV anode potential and a 20 mA filament emission current. Raman spectra were collected using a 532 nm laser excitation, utilising a $50 \times$ objective lens under a laser power of 6 mW. A custom-built UV-Vis spectroscope was also used to evaluate the electrochromic performance of different samples, via acquiring the transmittance spectra.[23] Light sourced from an incandescent bulb was focused onto the sample *via* a condenser lens which was collected by a $20 \times$ microscopy objective (Olympus MPLFLN, NA 0.45). After passing though the sample, the light was recorded on a spectrometer (Princeton Instruments Acton SP2500) once it reached the entrance slit. The spectrometer was equipped with a 1200 g/mm grating and a CCD camera (Princeton instruments PIXIS400). A Princeton Instruments IntelliCal system was used to calibrate and determine the efficiencies of optics and gratings at different wavelengths. A Keithley 2400 Source Meter was used to generate the bias voltage to the device. For the electrochemistry measurement, a CHI 760D potentiostat was used along with a standard three-electrode cell in which a Pt wire, the tungsten oxide thin films and an Ag/AgCl acted respectively as the courter, working and reference electrode. 0.5 M $LiClO_4$ and 4 w/v% of Polypropylene (PPC, average $M_n \sim 50000$) in propylene carbonate (PC) were utilised together as the gel electrolyte in all the cases.

Results and discussion

*Structure and morphology*

Comparison of SEM images between the pristine WO_x nanowires and the Ce-doped WO_x nanostructures (Figure 1) reveals that the lengths of the bundle and the morphology of WO_x were influenced significantly by the addition of Ce, varying with the Ce concentrations utilised during the synthesis. As shown in Figure 1a, the un-doped WO_x bundles were up to 2 µm long and about 20 nm in diameter. At the doping level of Ce/W = 1:15, the nanowires became shorter in length but thicker in diameter, which became more evident at higher doping levels (Ce/W = 1:10). Eventually agglomerates of very short nanowires were formed at Ce/W = 1:5, as shown in Figures 1b-1d.
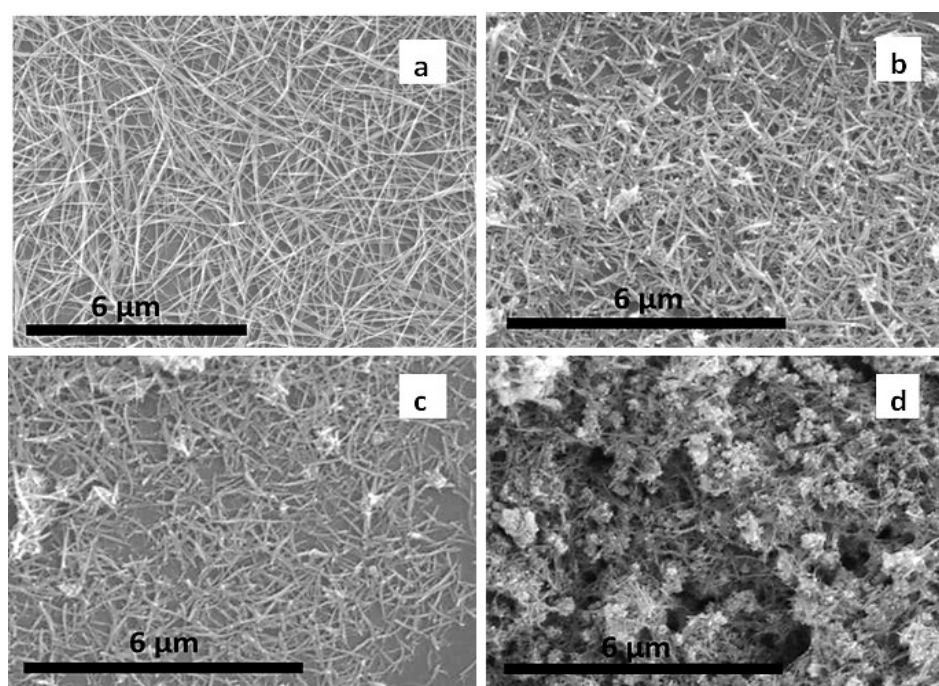
Figure 1. SEM images of: (a) the pristine $W_{18}O_{49}$ nanowire bundles, and (b-d) the Ce doped WO_x nanostructures, with Ce/W molar ratios of 1:15, 1:10, and 1:5, respectively.

XRD patterns of un-doped and doped samples (Figure 2) all matched well with ICDD No: 01-073-2177, confirming the dominant base crystalline feature of the $W_{18}O_{49}$ monoclinic phase, with lattice constants of a = 0.1832, b = 0.379, c = 1.404 nm and β = 115.03°. Two main diffraction peaks at about 23.5° and 47.5° (2θ) can be assigned to the (010) and (020) respectively, as shown in Figure 2.
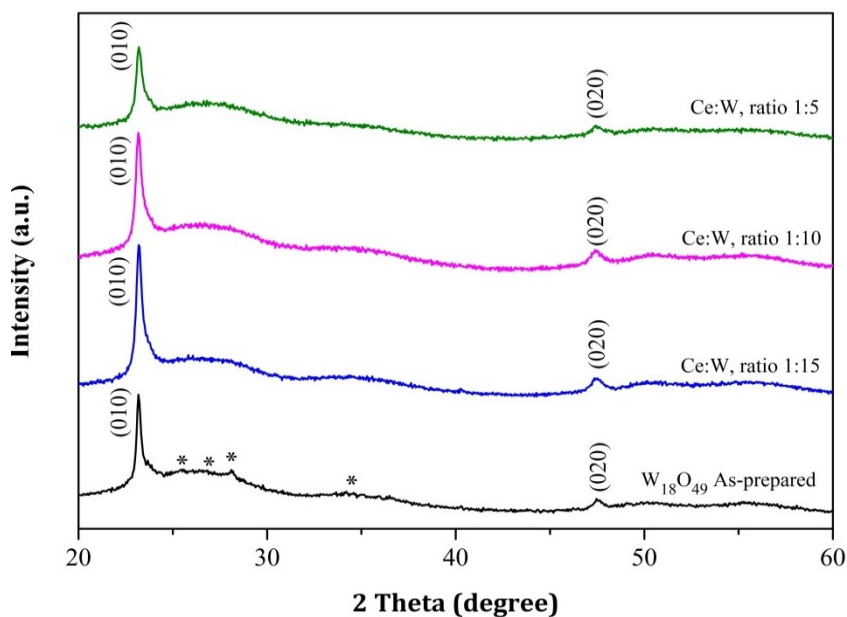
Figure 2. XRD patterns of as-synthesised nanomaterials corresponding to different Ce/W molar ratios.

The highest peak of the (010) plane indicated the preferential stacking of the (010) planes which corresponds to the <010> direction and aligns to the nanowire axis. This, along with the very low peaks of other planes (as show as * peak in Figure 2), *e.g.* (210), (012), (310) and (113), indirectly confirmed the ultrafine feature of the nanowires. The Full-width at half-maximum (FWHM) of the (010) plane also showed greater values at higher Ce/W molar ratios, *i.e.* corresponding to their smaller size of nanowires. This result matched well with the SEM observations (Figure 1) that nanowires became shorter and wider at higher Ce concentrations. From the XRD results, we did not find stronger evidence for the changes in crystalline structure between the doped and un-doped samples. However, the main (010) peak position silently shifted toward lower 2-theta position with increased amount of Ce doping. The (010) peak positions are located at 23.2°, 22.7° and 22.4° for the 1:15, 1:10 and 1:5 Ce/W samples, respectively, suggesting an enlarged d value.

HR-TEM images (Figure 3 and Figure S2) confirmed the ultrafine feature of several overlapped individual nanowires, about 2-5 nm in diameter and up to 2 μm long. These individual nanowires

8

formed bundles naturally to reduce surface energy, which led to their apparent diameters in the SEM images much bigger, due to the limitation of SEM to resolute individual nanowires. The lattice spacing of pure $W_{18}O_{49}$ nanowires (Figure 3a) was about 0.379 nm, corresponding to the d value of the (010) plane. This was consistent with that the nanowire grew along the <010> direction in the monoclinic structure. The selected-area electron diffraction (SAED) pattern of the $W_{18}O_{49}$ also revealed that the nanowire grew along the <010> direction, and the weak streak lines perpendicular to the (010) planes were indicative of the bundled and overlapped feature of the nanowires. This feature also explained why the width of these nanowires shown in the image was much bigger than 5 nm.
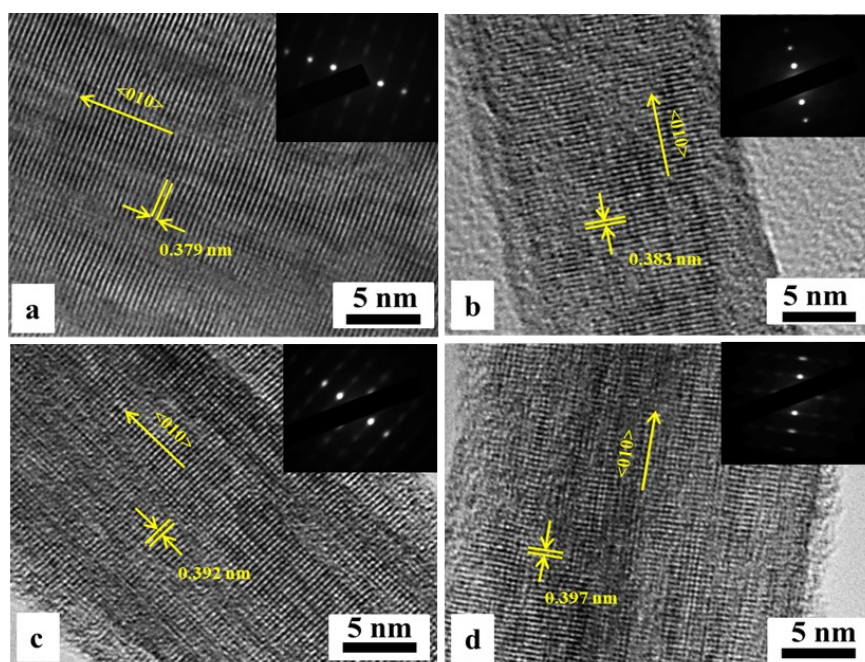
Figure 3. HRTEM images of differently doped nanowires and their corresponding SAED patterns: (a) Pure $W_{18}O_{49}$; (b) Ce/W = 1:15; (c) Ce/W = 1:10; and (d) Ce/W = 1:5.

From Figure 3, we noted a slightly increased (010) lattice spacing, by 1.1, 3.4 and 4.8%, for the differently doped nanowires, benchmarked against the plain $W_{18}O_{49}$ nanowires. The enlargement tendency appeared to be correlated with the increased Ce/W molar ratios (marked in Figure 3). Obviously, all the doped samples examined exhibited a single crystalline nature, similarly to the plain

200    $W_{18}O_{49}$, however the Ce incorporation into the structures had indeed resulted in a minor lattice

201   distortion, hence the enlarged d values. The TEM observations are in consistent with the left-shift of

202   the (010) peaks in the XRD results shown in Figure 2.

203   Chemical compositions of the samples were examined using XPS, and the results are shown in Figure

204   4. Due to the ultrafine diameter nature of the nanowires, the surface composition characteristic was

205   believed to be a logical reflection of the compositional feature of the nanowires. For plain $W_{18}O_{49}$

206   nanowires, the chemical state of core-level W 4f could be fitted into two spin-orbit doublets, which

207   were attributed to two different states of oxidation of the W atoms. The main doublets, with binding

208   energy for W $4f_{5/2}$ at 38.56 eV and W $4f_{7/2}$ at 36.43 eV, were associated with the W atoms in the W^{6+}

209   normal oxidation state. The other doublets at the electron binding energies of W $4f_{5/2}$ at 37.04 eV and

210   W $4f_{7/2}$ at 34.91 eV in Figure 4c could be identified as the W^{5+} oxidation state. The W 4f peak shifted

211   towards lower binding energy with the doping of Ce ions into the structure. To make the variation of

212   W^{6+} content more clearly, the ratio of W^{5+}/W^{6+}, which is approximate to the ratio of fitting peak areas,

213   was calculated and listed in Table 1.

214

215   Figure 4b are Ce 3d XPS spectra, corresponding to different molar ratios used during the synthesis.

216   Both oxidation states of Ce^{3+} and Ce^{4+} coexisted on the surface of ceria-containing samples, but the

217   former accounted for the main part of the ceria, due to the higher intensity and larger area in the

218   former than in the latter. At the lowest concentration of Ce-doped in the WO_x samples (prepared at

219   Ce/W = 1:15), the two peaks located at ~886 eV and ~905 eV were assigned to Ce^{3+} $3d_{5/2}$ and

220    $Ce^{3+}3d_{3/2}$ respectively, whilst those at ~882 eV and ~901eV were associated with the Ce^{4+} oxidation

221   state.[24, 25] At the intermediate and highest molar ratios of 1:10 and 1:5, the peak positions shifted

222   slightly towards the higher binding energy 886.35 eV and 905.39 eV, and 885.95 eV and 904.65 eV

223   for the Ce^{3+} $3d_{5/2}$ and Ce^{3+} $3d_{3/2}$ respectively; and accompanied with 882.54 eV for Ce^{4+} $3d_{5/2}$, 901.49

224   eV for Ce^{4+} $3d_{3/2}$, and 882.44 eV and 901.19 eV for the Ce^{4+} oxidation state, respectively.

Figure 4. (a) XPS survey spectra, high resolution scan of (b) Ce 3d, (c) W 4f and (d) O 1s of un-doped and doped samples.

The results in Table 1 show that the atomic ratios of W/O decreased with increasing the concentration of Ce ions inside the structures. Moreover, the increase of W^{5+}/W^{6+} ratios also indicated that the Ce^{3+} oxidation state of the Ce ions was reduced via charge transfer from the W ions, which resulted in the increase of W^{5+} oxidation state. The O 1s spectra (Figure 4d) showed two main peaks. The lower binding energy peak (530.3 - 530.8 eV) corresponded to the oxygen in the lattice and O^{2-} (peak 1), and the higher binding energy peak (532.4 - 532.7 eV) may be due to O^{2-}, O^-, and OH^- in the oxygen-deficient regions (peak 2).[26]

11

247 As understood from Table 1, Ce had been incorporated into the WO_x. It would be difficult for Ce^{4+}

248 and Ce^{3+} to replace the W in the lattice of $W_{18}O_{49}$ nanowires, because the ionic radii of Ce^{4+} (0.101

249 nm) and Ce^{3+} (0.103 nm) are much larger than those of W^{6+} (0.065 nm) and W^{5+} (0.068 nm).[12] It is

250 believed that the Ce cations might be inserted into the small tunnels of oxygen vacancy on the surface

251 and hexagonal channel of $W_{18}O_{49}$ structure. This analysis was supported by the XPS results shown

252 in Figure 4 which revealed the increase W^{5+} oxidation state and the higher binding energy shift of O

253 1s in peak 2, with respect to plain $W_{18}O_{49}$ samples. This O 1s shift in peak 1 towards the lower binding

254 energy also might be an evidence of more defective and weaker W-O bonding in the structure, as a

255 result of the Ce addition. Changing of this O 1s might be caused due to the lower electronegativity of

256 Ce than that of O. However, it is suggested that the Ce cations can facilitate the electron transfer and

257 the oxygen mobility in the doped samples, as confirmed by the altered states based on the XPS results.

258 The decreased atomic contents of W/O (Table 1), and the changes in the oxidation state as revealed

259 by the W 4f (from W^{6+} to W^{5+}) and Ce 3d spectra (from Ce^{4+} to Ce^{3+}) upon subsequent reduction,

260 both indicated the increase in oxygen vacancies and the release of free electrons in the doped

261 crystalline structures. The oxygen concentrations of doped samples shown in Table 1 are going down

262 and all lower than that of the plain $W_{18}O_{49}$ (0.79). The no linear trend for samples with Ce/W = 1:10

263 and 1:5 is minimal (0.761 vs 0.764), and could originate from two reasons: firstly, the upper limit of

264 the Ce doping within the framework could be between Ce/W = 1:10 and 1:5, and secondly the

265 localised minute composition variation obtained during the XPS could be the other cause (system

266 error). Their detailed effects on the electronic structure of Ce-doped WO_x remain unclear and so need

267 to be further investigated by the future work.

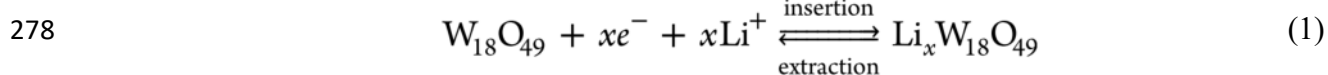268 **Table 1.** Surface characterization results from XPS.

Samples	Surface composition (atomic ratio)				
	Ce^{4+}/Ce^{3+}	W^{5+}/W^{6+}	$O_{total}/(O+Ce+W)$	$W_{total}/(O+Ce+W)$	$Ce_{total}/(O+Ce+W)$
Pure $W_{18}O_{49}$	-	0.102	0.790	0.21	-
Ce/W = 1:15	0.78	0.207	0.785	0.185	0.03
Ce/W = 1:10	0.57	0.157	0.761	0.196	0.043
Ce/W = 1:5	0.72	0.175	0.764	0.160	0.076

269

Electrochemical and electrochromic properties

Electrochromic properties of the Ce-doped thin film samples were evaluated by the CV technique, and compared with those of pure bundled $W_{18}O_{49}$ nanowire thin films (Figure 5). During each scan cycle, the films endured a typical reversible colour change, from blue to transparent, *i.e.* the coloration and bleached states. The recorded current was due to the intercalation/de-intercalation of Li^+ from the electrolyte and the electron transfer between W^{6+} and W^{5+} (as well as W^{4+} to W^{5+}), according to the following Equation 1 and 2, resepctively.[27, 28]

$$W_{18}O_{49} + xe^- + xLi^+ \underset{\text{extraction}}{\overset{\text{insertion}}{\rightleftharpoons}} Li_xW_{18}O_{49} \tag{1}$$

$$W^{5+}(A) + W^{6+}(B) + \text{photon} \rightarrow W^{6+}(A) + W^{5+}(B)$$

and $\quad W^{4+}(A) + W^{5+}(B) + \text{photon} \rightarrow W^{5+}(A) + W^{4+}(B) \tag{2}$

According to Figure 5, the area of the voltammogram was increased with the increase of scan rate, and the anodic peak current values were shifted towards higher potentials. The effective diffusion coefficient of Li^+ (D_{Li^+}) was calculated according to Randles-Sevick's equation (Equation 3), by assuming a simple solid state diffusion controlled process.[29, 30]

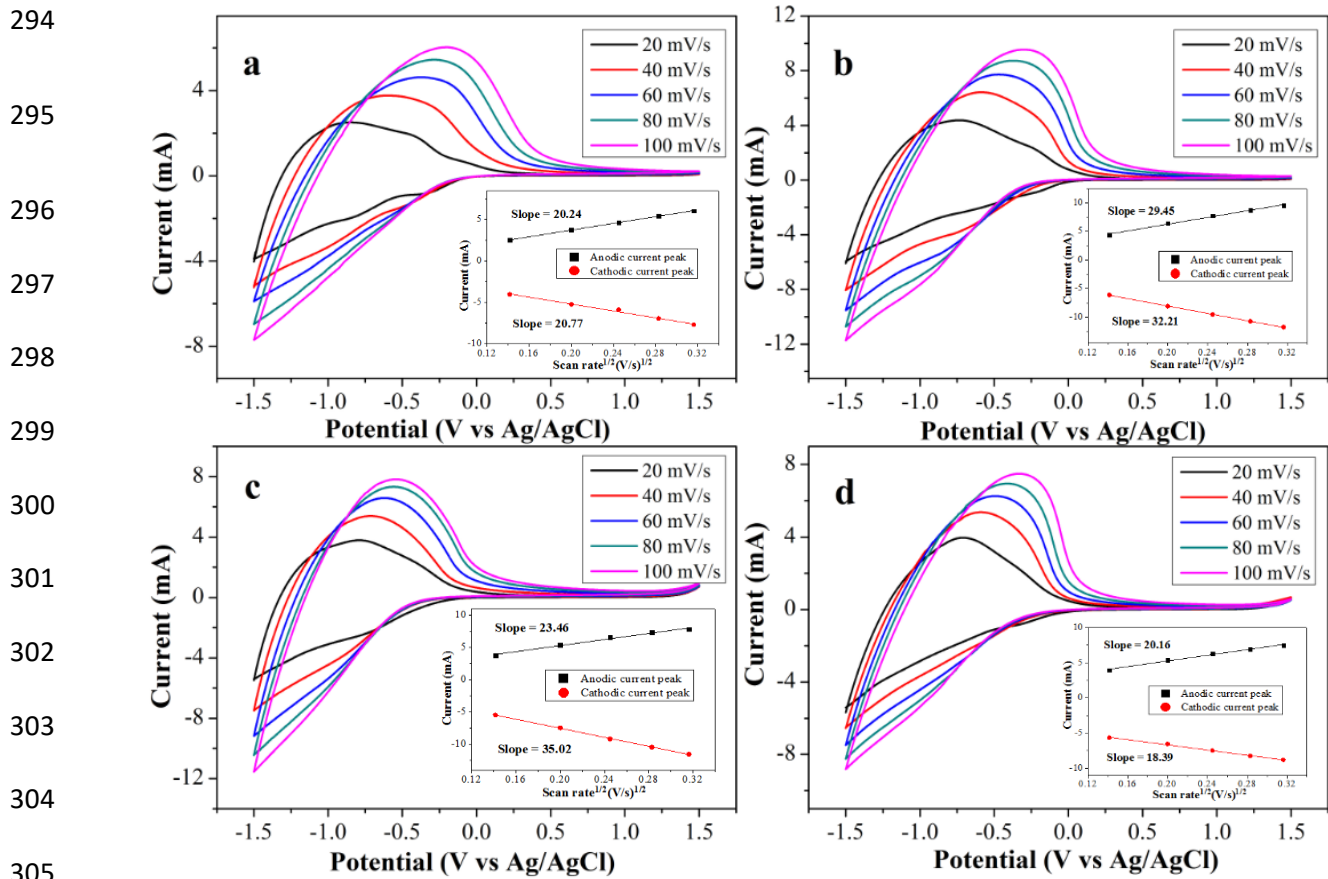$$D^{1/2} = \frac{i_p}{2.69 \times 10^5 \times n^{3/2} \times A \times C_o \times v^{1/2}} \tag{3}$$

where i_p is the peak current density, n the number of electrons transferred in unit reaction (n = 1 in this case),[31] A the surface area of the electrode film, C_0 the concentration of the diffusion species Li^+ (Mol/cm^3), and v the scan rate (V/s).

Figure 5. CV curves of different nanowire thin films: (a) Pure $W_{18}O_{49}$, (b) Ce/W = 1:15, (c) Ce/W = 1:10, and (d) Ce/W = 1:5. All results were recorded between -1.5 and 1.5 V at different scan rates of 20, 40, 60, 80 and 100 mV/s, using propylene carbonate (PC) with 0.5 M LiClO$_4$ and 4 w/v% PPC. Insets: the anodic and cathodic peak current density as a function of the square root of the scan rates.

Figure 5 shows the area of the voltammograms increased with increasing the scan rate. An anodic peak (which presented in positive current region) shifted towards higher potentials as the scan rate increases. The peak current *vs.* $v^{1/2}$ had been plotted using maximum and minimum current value (inside four CV graphs) and its slopes used to estimate D_{Li}^+ of all cases, according to Equation 3. The calculated D_{Li}^+ of intercalation/de-intercalation are $6.1 \times 10^{-10}/5.8 \times 10^{-10}$ cm^2/s, $1.5 \times 10^{-9}/1.23 \times 10^{-9}$ cm^2/s, $1.74 \times 10^{-9}/7.9 \times 10^{-10}$ cm^2/s and $4.8 \times 10^{-10}/5.8 \times 10^{-10}$ cm^2/s for the plain $W_{18}O_{49}$, Ce/W = 1:15, 1:10 and 1:5 samples, respectively. Higher intercalation than de-intercalation D_{Li}^+ values are obtained in all cases, and this might be due to the trapping of charge carriers inside the lattice

14

319 structures.[32] To further find out the stability of these samples, we recorded the 1st and the 1000th cycle

320 of all samples, as shown in Figure 6. Using the maximum specific anodic and cathodic peak currents

321 obtained at a middle scan rate of 60 mV/s, we calculated the D_{Li}^+ values for intercalation and de-

322 intercalation, and the results were summarised Table 2.

323

324 As shown in Table 2, all the doped samples exhibited better ion diffusion kinetics than the plain

325 $W_{18}O_{49}$ nanowires. In case of the latter, the diffusion coefficient D_{Li}^+ was 8.2×10^{-10} cm^2/s for the

326 intercalation, but is was increased to 2.1×10^{-9}, 1.99×10^{-9}, and 1.32×10^{-9} cm^2/s, respectively, in the

327 case of three Ce-doped samples, at a given scan rate of 60 mV/s. The D_{Li}^+ value decreased with

328 increasing the Ce ion concentration. Similar trend was also observed for the D_{Li}^+ of de-intercalation.

329 Importantly, the D_{Li}^+ values of both intercalation and de-intercalation for the doped samples were

330 much higher than original $W_{18}O_{49}$, by 177%, 102% and 84% of 1:15, 1:10 and 1:5 respectively. From

331 Table 2, the difference in the D_{Li}^+ values between the 1st and the 1000th cycle also showed that higher

332 Ce dopant slightly decreased the stability in intercalation for the thin films, by 4% for Ce/W = 1:15,

333 10% for Ce/W = 1:10 and 12% for Ce/W = 1:5, compared with pure $W_{18}O_{49}$. The stability in de-

334 intercalation for the 1:10 and 1:5 samples appeared to be similar to the intercalation, which was

335 decreased marginally by 6% and 1% respectively, however the film with the lowest concentration

336 (1:15) was only 20% difference, which is *ca.* 48% improvement [(41%-21%)/41%] in Table 2)

337 against the plain $W_{18}O_{49}$.

338 The Ce/W = 1:15 samples offered the fastest ion diffusion kinetics and best stability among all doped

339 samples. This might be due to the decreased dimensions of the sample (Supporting Information,

340 Figures S1 and S2), which resulted in increased surface area, and reduced ion diffusion path distance,

341 whilst still preserved enough room in between the lattice for Li$^+$ intercalation and de-intercalation. As

342 for Ce/W = 1:10 and 1:5 samples, they suffered from heavier agglomeration, and their structures

343 became bigger, leading to longer diffusion path. Meanwhile, too many Ce ions in the lattice would

15

make it more difficult for the Li^+ to get into/out the structure cyclically. In addition, a large D_{Li}^+

means a great mobility of Li^+, leading to a shorter switch time between the coloured and bleached

states. Figure 7 presents different intensities of the 1st cycle of the coloured stage for all the thin film

samples, evidently demonstrating the fundamental effects of different Ce contents on the coloration,

which could offer useful insight for materials selection towards efficient electrochromic device

construction.

Table 2. List of D_{Li}^+ values for the doped and pure $W_{18}O_{49}$ thin film samples.

Samples	D_{Li}^+ of Intercalation (cm^2/s)			D_{Li}^+ of De-intercalation (cm^2/s)		
	1st cycle	1000th cycle	Difference between 1st and 1000th cycle (%)	1st cycle	1000th cycle	Difference between 1st and 1000th cycle (%)
Pure $W_{18}O_{49}$	8.2×10^{-10}	7×10^{-10}	15	5.05×10^{-10}	3×10^{-10}	41
Ce/W = 1:15	2.1×10^{-9}	1.7×10^{-9}	19	1.4×10^{-9}	1.1×10^{-9}	21
Ce/W = 1:10	1.99×10^{-9}	1.5×10^{-9}	25	1.02×10^{-9}	5.3×10^{-10}	47
Ce/W = 1:5	1.32×10^{-9}	9.6×10^{-10}	27	9.3×10^{-10}	5.4×10^{-10}	42
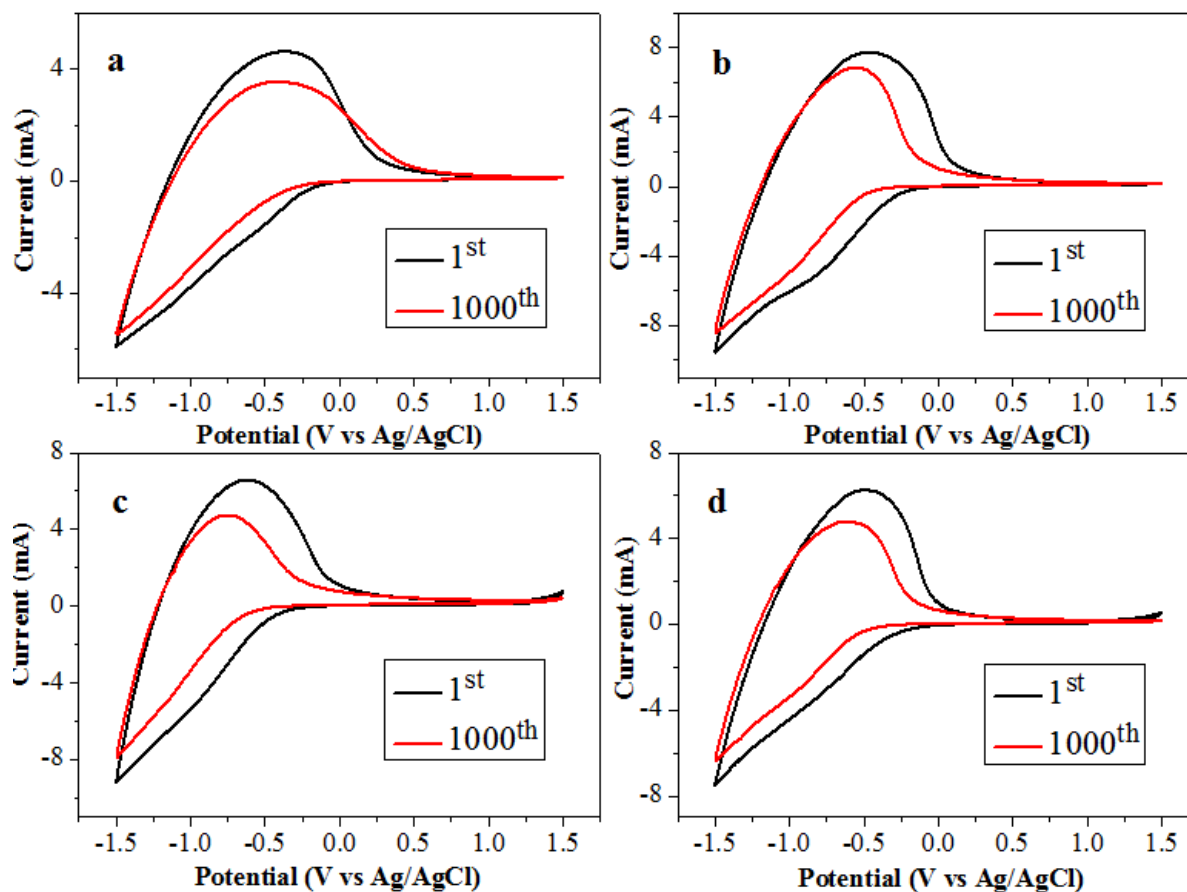
Figure 6. CV curves of different nanowire samples: (a) Pure $W_{18}O_{49}$, (b) Ce/W = 1:15, (c) Ce/W = 1:10 and (d) Ce/W = 1:5, after the 1st and the 1000th cycles, recorded between -1.5 and 1.5 V at 60 mV/s in all cases.
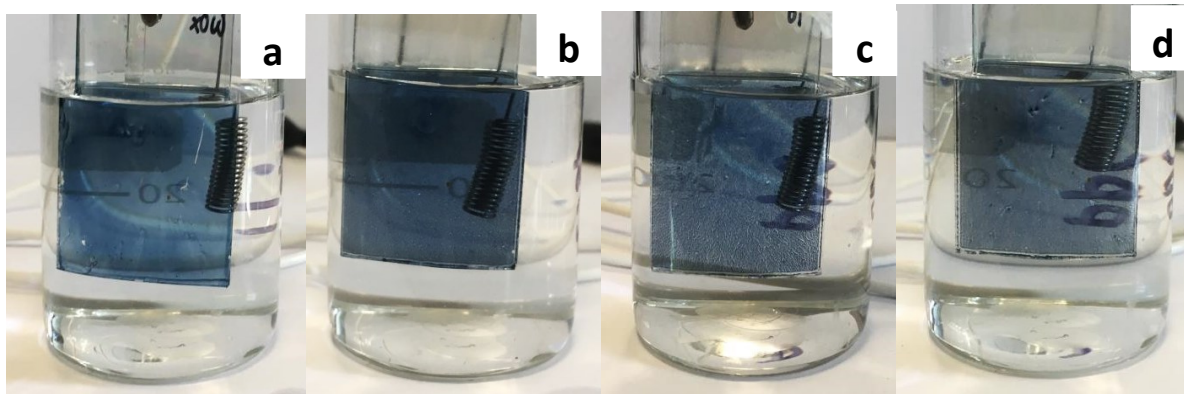
Figure 7. Visual observation of the coloured stage of various thin films: (a) pure $W_{18}O_{49}$, (b) Ce/W = 1:15, (c) Ce/W = 1:10, and (d) Ce/W = 1:5. The pictures were taken after the 1st cycle of CV testing between -1.5 and 1.5 V at 60 mV/s

The prototypes of electrochromic device for each sample were prepared for *in-situ* absorbance studies. The optical absorbance values of all the films were measured in the range from 430 to 750 nm in the coloured and bleached stages, subject to the intercalated or de-intercalated stages of Li$^+$ in the nanostructures. The optical contrast (ΔT) at a given specific wavelength of 630 nm (which is sensitive to human eyes) was calculated based on Equation 4.[30, 33]

$$\Delta T = [T_{bleched} - T_{coloued}]_{\lambda = 630 \text{ nm}} \quad (4)$$

As found from Table 3, the ΔT value increased by 2, 12.3 and 6.9% for Ce/W = 1:5, 1:10 and 1:15, respectively, in comparison with pure bundled $W_{18}O_{49}$ nanowires.

Table 3. Optical performance evaluated at 630 nm for the electrochromic prototypes constructed using Ce-doped WO_x and pure bundled $W_{18}O_{49}$ nanowires.

Sample	$T_{coloured}$ (%)	$T_{bleached}$ (%)	ΔT(%)	Q(C)	Q_d(C/cm^2)	ΔOD	CE (Colouration Efficiency, cm^2/C)
Pure $W_{18}O_{49}$	16.8	54.2	37.4	0.051	0.0083	0.51	61.9
Ce/W ratio 1:15	9.8	54.1	44.3	0.072	0.011	0.74	67.3
Ce/W ratio 1:10	20.4	70.1	49.7	0.05	0.008	0.53	66.3
Ce/W ratio 1:5	13.1	52.3	39.4	0.07	0.011	0.60	54.6

370

371
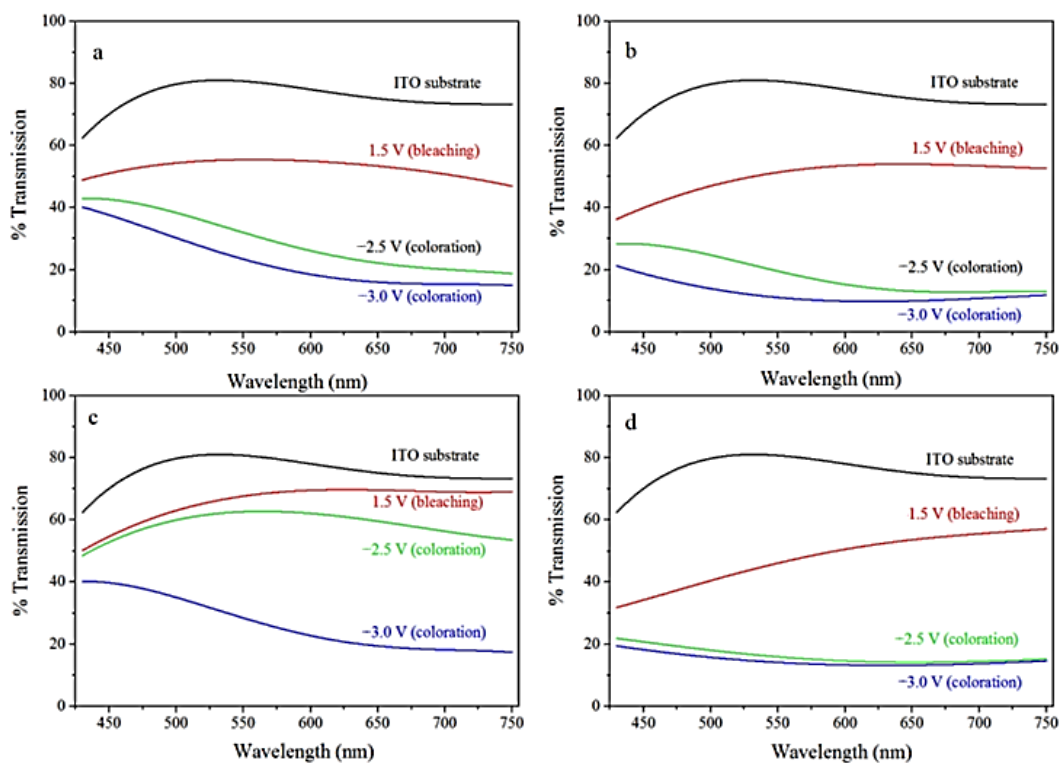
Figure 8. Transmission spectra in the visible range (from 400 to 750 nm) of (a) pure bundled $W_{18}O_{49}$ nanowires, (b) Ce/W = 1:15, (c) Ce/W = 1:10, and (d) Ce/W = 1:5 WO$_x$ thin films in their coloured and bleached states, on the application of different potentials ranging from +1.5 to -3.0 V.

375

Another important characteristic of chromic materials defining their suitability for real life applications is the Colouration Efficiency (CE), which represents the change in optical density (ΔOD) per the total charge passed across a unit area of the thin film (Q_d, C/cm^2), as defined by Equations 5 and 6.[34, 35]

18

$$CE = \frac{\Delta(OD)}{Q_d} \qquad (5)$$

where
$$\Delta OD(\lambda) = \log\left(\frac{T_{bleached}(\lambda)}{T_{coloured}(\lambda)}\right) \qquad (6)$$

Q_d is the amount of charge intercalated into the thin film samples, which can estimate by integrating the area under the curve current density versus time. Figure 8 gives the transmittance values of both the bleached and coloured states of each sample. Table 3 lists the optical contrast (ΔT), change of the optical density (ΔOD), charge density (Q_d) and colouration efficiency (CE) values for both the doped and un-doped samples. The percentages of optical contrast (%ΔT) of all the doped samples of different ratios were found to be better than the pure $W_{18}O_{49}$, being 39.4%, 49.7%, 44.3% and 37.4% for Ce/W = 1:5, 1:10, 1:15 and pure $W_{18}O_{49}$ nanowire thin films, respectively. The Ce/W = 1:15 thin film sample presented the highest OD value of 0.74 compared with pure $W_{18}O_{49}$ thin films (about 0.51). The CE corresponding to Ce/W = 1:5, 1:10, 1:15 and pure $W_{18}O_{49}$ was 54.6, 66.3, 67.3 and 61.9 cm^2/C, respectively. The sample with the lowest doping amount (1:15) showed the highest CE value than other two samples (1:10 and 1:5). It is believed that the Ce ions not only can induce/ oxygen vacancies in the lattice, but they can also occupy the oxygen vacant sites or/and bind with oxygen in the oxide lattice, to affect the content of W^{5+} (Table 1). Meanwhile, they can also enter the channels of the WO_x structures and blocks the free path of Li^+ and consequently reduces the Li^+ diffusion kinetics (D_{Li}^+), as shown in Table 2. A small but adequate amount of Ce doping in the structure could improve the performance of the oxide, however too many Ce ions could on one hand compete with the Li^+ for both the oxygen vacancies and free channels, and on the other hand block the path of Li^+ injection/de-injection during the coloration/bleaching reaction. Therefore, *via* such competition mechanisms, excessively higher Ce doping levels could lead to a negative effect on the overall electrochromic performance of the oxide.

Conclusion

Various Ce-doped WO_x nanostructures with molar ratios of Ce/W = 1:15, 1:10 and 1:5 in the precursors were successfully synthesised by using a simple solvothermal technique. The results showed that their morphologies had been modified compared with plain $W_{18}O_{49}$ ultrafine nanowires. The Ce-doped nanowires became shorter in length and larger in diameter with increasing the Ce concentration, and the sample with the highest Ce/W ratio of 1:5 exhibited the worst agglomerations among the short nanowires. XRD analyses on the $CeWO_x$ did not show obvious peak shifts, indicating that the $CeWO_x$ still retained the same basic monoclinic crystalline structure, akin to the plain $W_{18}O_{49}$, however the spectra of Ce 3d from XPS and the increased d values revealed by HRTEM both confirmed that Ce had been incorporated into the lattice of WO_x by occupying the vacant sites and channels. These doped Ce ions caused distortions in the crystal structures, modified the nanowire growth, and affected the amount of W^{5+}, and consequently affect the electrochromic performance of the nanowires. The thin film sample with lowest doping level (Ce/W = 1:15) showed the highest intercalation D_{Li^+} (2.1×10^{-9} cm^2/s) and de-intercalation D_{Li^+} (1.41×10^{-9}) at 60 mV/s, the better optical contrast (44.3%), the greatest CE (67.3 cm^2/C), and best de-intercalation stability (by 48%), amongst all doped and pure $W_{18}O_{49}$ samples. The distorted and enlarged structure favoured Li^+ intercalation/de-intercalation into/out of the structure during the redox reaction. The competition between the increased oxygen vacancies and available free pathway for Li^+ at various Ce contents is believed to be the reason for the overall best performance of the Ce/W = 1:15 thin film samples. These findings demonstrate that the Ce dopant offers an efficient and effective strategy for developing high optical contrast, short response time, high coloration efficiency and stable electrochromic devices, based on the novel $W_{18}O_{49}$ nanostructures. This work may contribute to the future development of WO_x-based multifunctional smart electrochromic devices for energy-related applications.

Conflicts of interest

There are no conflicts to declare.

Acknowledgements

References

[1] K. H. Krishna, O. M. Hussain and C. M. Julien, *Appl. Phys. A,* 2010, **99**, 921-929.

[2] P. J. Wojcik, L. Santos, L. Pereira, R. Martins and E. Fortunato, *Nanoscale*, 2015, **7**, 1696-1708.

[3] C. H. Lu, C. Y. Kuan and I. C. Leu, *J. Mater. Sci.*, 2015, **50**, 5739-5745.

[4] S. J. Yoo, J. W. Lim, Y. E. Sung, Y. H. Jung, H. G. Choi and D. K. Kim, *Appl. Phys. Lett.,* 2007, **90**, 173126.

[5] H. S. Shim, J. W. Kim, Y. E. Sung and W. B. Kim, *Sol. Energ. Mat. Sol. Cells*, 2009, **93**, 2062-2068.

[6] X. Chang, S. Sun, X. Xu and Z. Li, *Mater. Lett*., 2011, **65**, 1710-1712.

[7] S. Sun, Y. Zhao, Y. Xia, Z. Zou, G. Min and Y. Zhu, *Nanotechnology*, 2008, **19**, 305709.

[8] S. H. Mohamed and A. Anders, *Thin Solid Films*, 2007, **515**, 5264-5269.

[9] S. Luo, G. Fu, H. Chen and Y. Zhang, *Mater. Chem. Phys*., 2008, **109**, 541-546.

[10] N. D. Zakharov, P. Werner, I. P. Zibrov, V. P. Filonenko and M. Sundberg, *J. Solid State Chem*., 1999, **147**, 536-544.

[11] M. A. Yar, S. Wahlberg, M. O. Abuelnaga, M. Johnsson and M. Muhammed, *J. Mater. Sci.*, 2014, **49**, 5703-5713.

[12] X. Chang, S. Sun, Y. Zhou, L. Dong and Y. Yin, *Nanotechnology*, 2011, **22**, 265603.

[13] M. Chuai, Q. Zhao, T. Yang, Y. Luo and M. Zhang, *Mater. Lett*., 2015, **161**, 205-207.

455 [14] B. Chouchene, T. Ben Chaabane, L. Balan, E. Girot, K. Mozet, G. Medjahdi and R. Schneider,

456 *Beilstein J. Nanotechnol.*, 2016, **7**, 1338-1349.

457 [15] S. Muthukumaran and R. Gopalakrishnan, *J. Sol-Gel Sci. Technol.*, 2012, **62**, 193-200.

458 [16] L. Chen, J. Li and M. Ge, *J. Phys. Chem.*, 2009, **113**, 21177-21184.

459 [17] M. Dhanasankar, K.K. Purushothaman and G. Muralidharan, *Mater. Res. Bull.*, 2010, **45**,

460 1969-1972.

461 [18] A. K. Bhosale, S. R. Kulal, V. M. Gurame and P. S. Patil, *Bull. Mater. Sci.*, 2015, **38**. 483-491.

462 [19] A. Verma, A. K. Srivastava, A. K. Bakhshi, R. Kishore and S. A. Agnihotry, *Mater. Lett.*,

463 2005, **59**, 3423-3426.

464 [20] A. W. Xu, Y. Gao and H. Q. Liu, *J. Catal.*, 2002, **207**, 151-157.

465 [21] W. Shan, Y. Geng, X. Chen, N. Huang, F. Liu and S. Yang, *Catal. Sci. Technol.*, 2016, **6**,

466 1195-1200.

467 [22] P. Muthukumaran, C. V. Raju, C. Sumathi, G. Ravi, D. Solairaj, P. Rameshthangam, J. Wilson,

468 S. Rajendran and S. Alwarappan, *New J. Chem.*, 2016, **40**, 2741-2748.

469 [23] A. D. Sanctis, G. F. Jones, N. J. Townsend, M. F. Craciun and S. Russo, *Rev. Sci. Instrum.*,

470 2016, **88**, 055102.

471 [24] L. Wang, L. Zhuang, H. Xin, Y. Huang and D. Wang, *Inorg. Chem.*, 2015, **1**, 52981.

472 [25] R. Fiala, M. Vaclavu, A. Rednyk, I. Khalakhan, M. Vorokhta, J. Lavkova, V. Potin, I.

473 Matolinova and V. Matolin, *Catal. Today*, 2015, **240**, 236-241.

474 [26] L. Jiang, H. Zhub, R. Razzaq, M. Zhu, C. Li and Z. Li, *Int. J. Hydrogen Energy*, 2012, **37**,

475 15914-15924.

476 [27] J. Zhu, M. Vasilopoulou, D. Davazoglou, S. Kennou, A. Chroneos and U. Schwingenschlogl,

477 *Sci. Rep.*, 2017, **7**, 40882.

478 [28] M. Meenakshi, R. Sivakumar, P. Perumal and C. Sanjeeviraja*, Mater. Today: Proceeding*,

479 2016, **3S**, S30-S39**.**

480   [29] Z. Jiao, J. Wang, L. Ke, X. Liu, H. V. Demir, M. F. Yang and X. W. Sun, *Electrochim. Acta*,

481   2012, **63**, 153-160.

482   [30] S. S. Kalagi, S. S. Mali, D. S. Dalavi, A. I. Inamdar, H. Im and P. S. Patil, *Electrochim. Acta*,

483   2012, **85**, 501-508.

484   [31] H. M. A. Soliman, A. B. Kashyout, M. S. E. Nouby and A. M. Abosehly, *J. Mater. Sci. Mater.*

485   *Electron*, 2010, **21**, 1313-1321.

486   [32] B. E. Francisco, C. R. Stoldt and J. C. M'Peko, *Chem. Mater.*, 2014, **26**, 4741-4749.

487   [33] H. Chen, N. Xu, S. Deng, J. Zhou, Z. Li, H. Ren J. Chen and J. She, *J. Appl. Phys.*, 2007, **101,**

488   114303.

489   [34] J. Padilla and T. F. Otero, *Bioinspir. Biomim.*, 2008, **3**, 035006.

490   [35] M. Nunes, M. Araujo, J. Fonseca, C. Moura, R. Hillman and C. Freire, *ACS Appl. Mater.*

491   *Interfaces*, 2016, **8**, 14231-14243.